π^--^{12}C elastic scattering above the Δ resonance

T. Takahashi,[1] H. Sakaguchi,[1] K. Aoki,[2] T. Hasegawa,[3] O. Hashimoto,[3] T. Nagae,[3] M. Sekimoto,[3] A. Ohkusu,[4] H. Bhang,[5] H. Yu,[5] and Y. Gavrilov[6]

[1]*Department of Physics, Kyoto University, Kyoto 606-01, Japan*
[2]*National Laboratory for High Energy Physics (KEK), Ibaraki 305, Japan*
[3]*Institute for Nuclear Study, University of Tokyo, Tanashi 188, Japan*
[4]*Department of Physics, Osaka University, Toyonaka 660, Japan*
[5]*Department of Physics, Seoul National University, Seoul 151-742, Korea*
[6]*Institute for Nuclear Research, Academy of Science of Russia, Moscow, Russia*

(Received 27 January 1995)

Systematic measurements of π^- elastic scattering on ^{12}C above the Δ-resonance region are reported. The differential cross sections were measured at 610, 710, 790, and 895 MeV/c over an angular range from 5° to 50°. The obtained data were compared with the first-order optical potential model. In the forward region, agreement with the calculation increases with the incident momentum. In the backward region, however, the calculation underestimates the data. The total cross section was extracted, and its energy dependence shows that the effect of Fermi averaging is important.

PACS number(s): 25.80.Dj, 24.10.Ht

I. INTRODUCTION

Recent theoretical studies suggest the possibility of using pions in the GeV/c region as a probe to investigate nuclear structures. The pion-nucleon interaction is very strong (200 mb for π^+p, 70 mb for π^-p) in the Δ-resonance region. As the incident momentum increases, the pion-nucleon cross section decreases and becomes 20–40 mb in the GeV/c region. Thus, the pions are supposed to be very transparent above the Δ-resonance region. Moreover, the elementary amplitude becomes forward peaked. Accordingly, the reaction process itself is also supposed to be simple.

In this energy region, pion elastic-scattering data on ^{12}C and ^{40}Ca at 800 MeV/c were measured at Brookhaven National Laboratory (BNL) [1]. The data have been qualitatively reproduced by a momentum-space calculation. However, the calculation underestimates the absolute magnitude of the experimental cross section. The discrepancy is larger than the absolute normalization error of the experiment.

Stimulated by these data, many theoretical investigations concerning pion-nucleus reactions in the GeV/c region have been carried out based on the optical potential model [2,3], Glauber theory [2,4,5], and the eikonal model [3]. These theoretical calculations have more or less agreed with each other and have underestimated the BNL data. In order to explain the difference, higher-order nuclear effects, such as nuclear correlation and pion absorption, have been taken into account. However, the discrepancy in the forward angles is still not fully understood [2].

In order to explain this discrepancy and to further explore the effectiveness of pions as a probe to investigate nuclear structures, we need to understand the reaction process both precisely and systematically. As for the experimental side, there have been only a few pion scattering data in this energy region: the BNL data on ^{12}C and ^{40}Ca at a pion incident momentum of 800 MeV/c (673 MeV kinetic energy) [1] and the LAMPF data at 400 and 500 MeV in kinetic energy [6]. This is because we need a high-resolution spectrometer for both beam and scattered particles in order to separate the elastic scattering from the inelastic scattering.

Here, we report on our systematic measurements of pion elastic scattering from ^{12}C at incident momenta of 610, 710, 790, and 895 MeV/c using a newly constructed Superconducting Kaon Spectrometer (SKS) [7]. The SKS provides us with a unique opportunity to carry out nuclear spectroscopy using meson beams in the GeV/c region. The main purpose of this experiment is to obtain systematic data on π^--^{12}C elastic scattering above the Δ-resonance region with well-controlled systematic errors. The incident momenta were chosen so as to investigate the effects of N^*'s (1440, 1520, 1535, 1680, ...) in the pion-nucleus scattering.

In Sec. II we describe the experimental apparatus while emphasizing the experimental setup and procedure specific to the elastic-scattering measurement. The procedures used to deduce the cross sections are explained in Sec. III. In Sec. IV we examine the reliabilities of our data, and compare the data with the first-order optical potential model calculation. A summary is given in Sec. V.

II. EXPERIMENTAL APPARATUS

The experiment was performed in the North Experimental Hall of the KEK Proton Synchrotron (PS) using the SKS. The negative pion beam momenta were 610, 710, 790, and 895 MeV/c. Figure 1 shows a schematic view of the experimental setup.

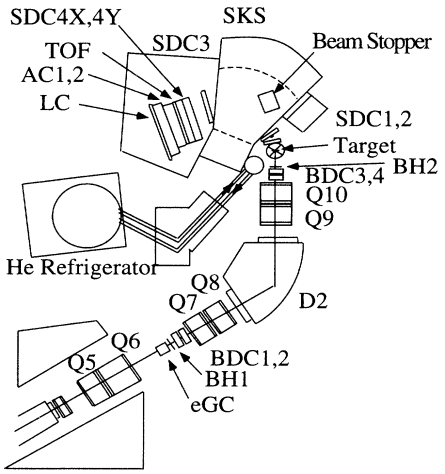

FIG. 1. Schematic view of the experimental setup.

A. Beam spectrometer

Pions produced at a production target (Pt, 6 mm diameter × 60 mm length) were delivered to the experimental target through the K6 beam line located in the north experimental area of the KEK PS. The beam momentum was analyzed with a beam spectrometer comprising a $QQDQQ$ system, high-rate drift chambers, timing hodoscope counters, and an electron gas Čerenkov counter (eGC).

Pions were selected with electrostatic separators in the K6 beam line. In addition, the time of flight (TOF) between two timing counters (BH1 and BH2) was used in an on-line trigger in order to reject heavier particles. The eGC was also used in order to reject electrons. The beam was counted particle by particle using a scaler. Further, muon contamination, which cannot be separated by the TOF, was measured in separated runs using a high-pressure freon gas Čerenkov counter (μGC) placed at the target position. The results given in Table I are consistent with the results of DECAY TURTLE [8]. The third column in the table represents the number of muons having a momentum above the threshold. Since the μGC is sensitive to muons with a momentum above the threshold, the simulated total number of muons (the last column in the table) was used to normalize the pion flux.

Four sets of drift chambers (BDC1–4), of ±2.5 mm cell size were installed upstream and downstream of the $QQDQQ$ system. The BDC's measured the beam trajectory with a position resolution of $\sigma \approx 250$ μm. The momentum of the π^- was obtained particle by particle using a third-order transport matrix. To calibrate the beam spectrometer and the SKS, the beam momentum was also measured with the SKS in separated runs; a correction has also been made.

B. Scattered-particle spectrometer (SKS)

Scattered pions were measured with the SKS, which is comprised of a large superconducting dipole magnet, drift chambers (SDC1,2,3,4X,4Y), and trigger counters. The spectrometer has a large acceptance (±15° horizontal and ±5° vertical, 100 msr in total) and a good momentum resolution [$\Delta p/p = 0.1\%$ full width at half maximum (FWHM)]. The trigger counters are comprised of a scintillator wall (TOF), two layers of aerogel Čerenkov counters (AC1,AC2), and a Lucite Čerenkov (LC) wall to reject protons. The trigger logic for scattered pions was TOF ⊗ LC. AC's were not used for this measurement. The momentum of a scattered particle was obtained by solving the equation of motion (Runge-Kutta method [9]) using the hit positions in the tracking drift chambers and a precisely measured magnetic field map.

SDC1 and SDC2, placed upstream of the dipole, had the same drift-cell structure as that of the BDC's. They

TABLE I. Ratio of the muons in the beam. The second column represents the experimental value measured with a gas Čerenkov counter. The third column represents the number of muons with a momentum above the threshold by a DECAY TURTLE simulation. The last column shows the total number of muons at the target.

Setup	Measured (%)	DECAY TURTLE (%)	
		Above threshold	Total
P_π=895 MeV/c			
Angular setup 1	4.1 ± 1.0	3.6 ± 0.2	5.9 ± 1.0
Angular setup 2	4.5 ± 1.0	3.9 ± 0.1	6.2 ± 1.0
P_π=790 MeV/c			
Angular setup 1	4.3 ± 1.0	3.8 ± 0.3	6.3 ± 1.0
Angular setup 2	4.8 ± 1.0	3.9 ± 0.3	6.5 ± 1.0
Angular setup 3	5.1 ± 1.0	4.1 ± 0.2	6.6 ± 1.0
P_π=710 MeV/c			
Angular setup 1	5.0 ± 1.0	4.0 ± 0.7	7.2 ± 1.0
Angular setup 2	4.9 ± 1.0	4.4 ± 0.6	7.4 ± 1.0
Angular setup 3	5.5 ± 1.0	4.3 ± 0.6	7.2 ± 1.0
P_π=610 MeV/c			
Angular setup 1	4.9 ± 1.0	4.2 ± 0.4	7.5 ± 1.0
Angular setup 2	5.1 ± 1.0	4.1 ± 0.4	7.4 ± 1.0
Angular setup 3	4.7 ± 1.0	4.1 ± 0.3	7.4 ± 1.0

could be operated at a high counting rate of up to approximately a few MHz. SDC3, $4X$, and $4Y$, which were installed at the exit of the magnet, had a wire spacing of 21 mm. Since pions scattered elastically have almost the same momentum as that of the beam, it is difficult to separate them from the beam by a magnetic field. This is a different situation from (π,K) measurements in the SKS or measurements using small-aperture spectrometers. The following points had to be considered for the present measurements: (1) To stop the beam before the downstream detectors, which could not accept a high counting rate. (2) To reduce background triggers caused by the beam hitting such materials as the spectrometer yoke and beam stopper. (3) Moreover, because the cross section at 5° is about 100 times as large as that at 25°, it was difficult to effectively accumulate sufficient statistics for the backward region in the same trigger condition.

We therefore used three detector setups according to scattering-angle range:

(i) Angular setup 1 (5°–20°). The SKS was positioned so that the central track was at 14°. A stack of lead blocks (30 $cm^W \times$ 40 $cm^H \times$ 50 cm^L) was installed in the gap of the dipole to stop the beam (unscattered particles).

(ii) Angular setup 2 (10°–25°). In the same position of the SKS as angular setup 1, a veto scintillator (SAV) was placed in front of SDC2 to reject triggers from particles scattered in the forward angles.

(iii) Angular setup 3 (25°–55°). The SKS was rotated to 39°. Since the beam was stopped at the yoke near to the entrance of the SKS, the beam stopper was removed.

C. Experimental procedure

A natural-carbon target of 10 cm×10 cm×0.89 (1.78) g/cm^2 was used for the measurement in the angular setup 1 (2,3). In order to examine the absolute normalization, we also measured the $\pi^- p$ elastic cross section using a scintillator target of 7 $cm^W \times$9 $cm^H \times$1.07 g/cm^2 (BICRON BC-408).

Since we needed both to stop as many beams as possible and to get reasonably small beam size at the target, the beam transport was tuned so as to focus the beam in between the target and the beam stopper. The size of beam at the target was typically 2 cm [X] × 4 cm [Y] (FWHM), while the horizontal and vertical angular distributions were about ±30 mrad and ±20 mrad (FWHM), respectively. Veto scintillators (TV) were installed on both sides of the target so as to reduce ineffective triggers caused by the tail components of the beam without hitting the target.

We adjusted the beam intensity in order to keep the data-acquisition dead time at less than 10%. A typical beam intensity was 4×10^5/spill, 1×10^6/spill, and 2×10^6/spill for measurements in angular setups 1, 2, and 3, respectively. The typical trigger rate was about 500–800 events/spill, where the spill interval was 4 sec and its duration was 1.2 sec.

III. PROCEDURES TO DEDUCE THE CROSS SECTION

In order to select events from π^--^{12}C scattering, the following software cuts were applied:

(1) A multiplicity of one was required in all hodoscope trigger counters (BH1, BH2, TOF, LC).

(2) The TOF between BH1 and BH2 was required to be within the window for pions.

(3) Tracks upstream and downstream of $QQDQQ$ in the beam spectrometer were reconstructed with a reasonable χ^2 value.

(4) The direction of the beam was within the defined windows (±70 mrad in horizontal and ±40 mrad in vertical).

(5) The TOF between the TOF and LC counters was required to be within reasonable windows.

(6) A track in the SKS was reconstructed with a reasonable χ^2 value.

(7) An event vertex was required to be within the target volume.

As shown in Fig. 2, a Z projection of the event vertex (Z axis is taken to the beam direction) shows a clear separation from the background.

The scattering angle was determined based on the trajectories of both spectrometers with 0.2° (rms) angular resolution. The excitation energy was calculated based on the scattering angle and momenta measured with both spectrometers. In the calculation of the excitation energy, the energy loss in the target was corrected assuming that the pion was scattered at the half depth of the target. Figure 3 shows the excitation energy spectra with

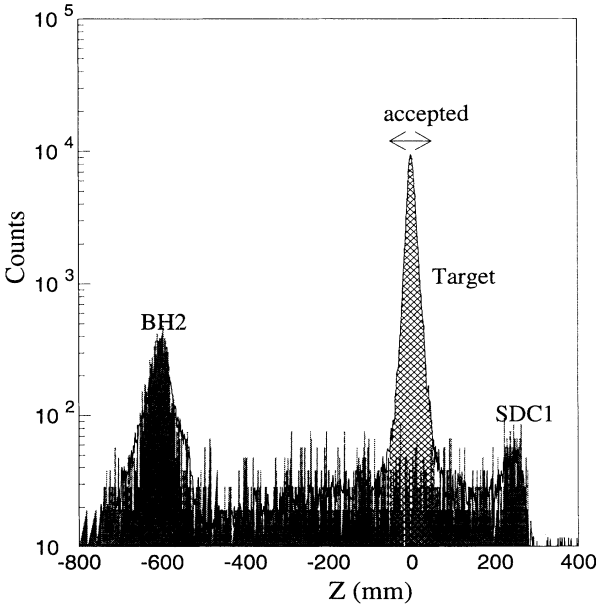

FIG. 2. Z projection of the event vertex. The events scattered at the target and BH2 can be distinguished. A cut of -50 mm $\leq Z \leq$ 50 mm (hatched area) was applied. The shadow histogram represents the background measured in an empty target run.

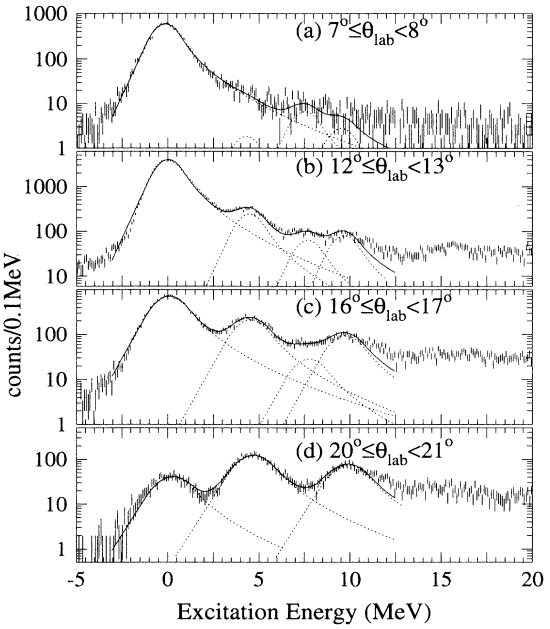

FIG. 3. Excitation energy spectra at $P_{\rm lab}$=790 MeV/c. The histogram is summed in the scattering-angle range (a) from 7° to 8°, (b) from 12° to 13°, (c) from 16° to 17°, and (d) from 20° to 21°, respectively. The solid curves show the results of fitting. The dotted curves show individual peaks.

an energy resolution of about 2 MeV (FWHM).

Taking account of the efficiencies due to various software cuts, the differential cross section is expressed as follows:

$$\frac{d\sigma}{d\Omega}(\theta) = Y(\theta)\frac{1}{N_{\rm tgt}N_{\rm beam}}\frac{1}{\Delta\Omega_{\rm eff}(\theta)}\frac{1}{\varepsilon(\theta)}, \quad (1)$$

$$N_{\rm beam} = N_{\rm sca}\varepsilon_{\rm K6\ cut}R_{\pi\mu}, \quad (2)$$

$$\Delta\Omega_{\rm eff}(\theta) = \Delta\Omega(\theta)\varepsilon_{\rm decay}(\theta)(1-\varepsilon_{\rm abs}), \quad (3)$$

$$\varepsilon(\theta) = \varepsilon_{\rm K6}\varepsilon_{\rm SKS}(\theta)\varepsilon_{\rm vertex}\varepsilon_{\rm DAQ}, \quad (4)$$

$$\varepsilon_{\rm K6} = \varepsilon_{\rm BDC}\varepsilon_{\rm BH1-BH2}\varepsilon_{\rm K6\ track}, \quad (5)$$

$$\varepsilon_{\rm SKS}(\theta) = \varepsilon_{\rm SDC12}(\theta)\varepsilon_{\rm SDC34}\varepsilon_{\rm TOF-LC} \times\varepsilon_{\rm SKS\ track}(\theta)\varepsilon_{\rm SKS\ cut}(\theta). \quad (6)$$

Here, $Y(\theta)$ is the yield at the scattering angle (θ), $N_{\rm tgt}$ the target areal density, $N_{\rm beam}$ is the pion flux, $N_{\rm sca}$ the scaler counts of BH1×BH2×$\overline{\rm eGC}$, $R_{\pi\mu}$ the ratio of pions to beam, $\Delta\Omega_{\rm eff}(\theta)$ the effective solid angle, and $\varepsilon(\theta)$ the experimental and/or analysis efficiency. The definitions of the efficiencies are listed Table II.

A. Peak fitting

On each 1° scattering angle bin, the yields were extracted by fitting the spectrum with four peaks (corresponding to ground state, 2_1^+, 0_2^+, and 3_1^- states). The background level is lower than these four peaks, as shown in Fig. 3. The peak shape was defined at forward angles, where the strength of inelastic scattering is less than 1% of the elastic scattering. We compared χ^2 and the peak area with the following three types of shapes. These shapes are Gaussian with different asymmetric tails:

$$\text{shape 1}: f_1(x) = \begin{cases} a\exp\left\{\frac{3}{2}\frac{(x-p)}{\sigma}+\frac{9}{8}\right\} & (x \le p-\frac{3}{2}\sigma), \\ a\exp\left\{-\frac{(x-p)^2}{2\sigma^2}\right\} & (p-\frac{3}{2}\sigma < x \le p+\sigma), \\ a\exp\left\{-\frac{x-p}{\sigma}+\frac{1}{2}\right\} & (p+\sigma < x \le p+\frac{3}{2}\sigma), \\ a\sqrt{\frac{3\sigma}{2(x-p)}}\exp\left\{-2\sqrt{\frac{2(x-p)}{3\sigma}}+1\right\} & (p+\frac{3}{2}\sigma < x); \end{cases}$$

$$\text{shape 2}: f_2(x) = \begin{cases} a\exp\left\{-\frac{(x-p)^2}{2\sigma^2}\right\} & (x \le p+\sigma), \\ a\exp\left\{-\frac{x-p}{\sigma}+\frac{1}{2}\right\} & (p+\sigma < x \le p+\frac{3}{2}\sigma), \\ a\sqrt{\frac{3\sigma}{2(x-p)}}\exp\left\{-2\sqrt{\frac{2(x-p)}{3\sigma}}+1\right\} & (p+\frac{3}{2}\sigma < x); \end{cases}$$

$$\text{shape 3}: f_3(x) = \begin{cases} a\exp\left\{-\frac{(x-p)^2}{2\sigma^2}\right\} & (x \le p+\sigma), \\ a\exp\left\{-\frac{x-p}{\sigma}+\frac{1}{2}\right\} & (p+\sigma < x). \end{cases}$$

In the fitting, the energy differences (4.44, 7.65, and 9.64 MeV) were fixed, and the same width parameter (σ) was used for all four peaks.

As shown in Table III, shape 1 gives the smallest χ^2. The difference of the area among three shapes is less than 4%. Therefore, shape 1 was adopted to extract the yield at other scattering angles. Further, the systematic error due to the choice of the peak shape was estimated to be about 4%. The uncertainty of the peak area calculated from the error matrix is almost the same as the square root of the peak area.

For πp scattering, the spectrum was fitted with a single peak after subtracting the background from carbon by using carbon data (Fig. 4).

B. Experimental efficiencies

In order to deduce the absolute magnitude of the cross section, it is necessary to obtain all of the efficiencies precisely. There are two types of efficiencies: One is the intrinsic efficiency of each detector; the other is the analysis efficiency due to the analysis algorithm and software cuts, etc. For the tracking detectors, the effect of the former was negligible compared to the latter, since we had so many redundant planes in the tracking chambers. For the TOF and LC, the intrinsic efficiencies were more than 99.8%, and were negligible.

Each analysis efficiency was estimated with the obtained data as follows:

$$\varepsilon = \frac{\text{number of events accepted in the analysis}}{\text{number of selected events to be analyzed}}. \quad (7)$$

TABLE II. Definition of the experimental efficiency factors. The typical value was taken from a 790 MeV/c angular setup 2 measurement.

Factor	Meaning	Typical value (%)	Relative error (%)
$\varepsilon_{\mathrm{K6}}$	Beam line spectrometer's efficiency	73.3 ± 2.0	2.7
$\varepsilon_{\mathrm{SKS}}(\theta)$	SKS spectrometer's efficiency	58.3 ± 4.2[a]	7.2
$\varepsilon_{\mathrm{vertex}}$	Event vertex cut efficiency (cut 7)	99.0 ± 1.0	1.0
$\varepsilon_{\mathrm{DAQ}}$	Data-acquisition efficiency	90.2 ± 0.1	0.1
$\varepsilon_{\mathrm{K6\ cut}}$	Beam profile cut efficiency (cuts 2,4)	83.2 ± 0.7	0.8
$R_{\pi\mu}$	Ratio of pions to beam	93.5 ± 2.0	2.1
$\varepsilon_{\mathrm{decay}}$	Pion survival rate	[b]	
$\varepsilon_{\mathrm{abs}}$	Pion absorption rate in detectors	7.3 ± 1.0	1.1
$\varepsilon_{\mathrm{BDC}}$	BDC (analysis) efficiency	79.8 ± 1.0	1.3
$\varepsilon_{\mathrm{BH1-BH2}}$	Analysis efficiency of beam line trigger counters (BH1,BH2) (cut 1)	98.4 ± 0.5	0.5
$\varepsilon_{\mathrm{K6\ track}}$	Analysis efficiency of beam momentum reconstruction (cut 3)	86.8 ± 0.6	0.7
$\varepsilon_{\mathrm{SDC12}}(\theta)$	SDC12 analysis efficiency	77.0 ± 4.0	5.2
$\varepsilon_{\mathrm{SDC34}}$	SDC34 analysis efficiency	94.5 ± 1.0	1.1
$\varepsilon_{\mathrm{TOF\text{-}LC}}$	Analysis efficiency of SKS trigger counters (TOF,LC) (cuts 1,5)	95.8 ± 0.5	0.5
$\varepsilon_{\mathrm{SKS\ track}}(\theta)$	Analysis efficiency of SKS momentum reconstruction	98.3 ± 3.0[a]	3.1
$\varepsilon_{\mathrm{SKS\ cut}}(\theta)$	Software cut efficiency in the SKS (cut 6)	85.1 ± 3.0[a]	3.5

[a]A value at 14.5° scattering angle which correspond to central trajectory.
[b]Unknown in our estimation. See the text.

All of the efficiencies in the beam line ($\varepsilon_{\mathrm{BDC}}$, $\varepsilon_{\mathrm{BH1-BH2}}$, $\varepsilon_{\mathrm{K6\ track}}$, and $\varepsilon_{\mathrm{K6\ cut}}$) were estimated using beam-trigger data in order to avoid a trigger bias. Typical values of $\varepsilon_{\mathrm{BDC}}$, $\varepsilon_{\mathrm{BH1-BH2}}$, $\varepsilon_{\mathrm{K6\ track}}$, and $\varepsilon_{\mathrm{K6\ cut}}$ were (80±1)%, (98±1)%, (90±1)%, and (80±1)%, respectively.

For $\varepsilon_{\mathrm{SDC34}}$, using the hit information of the TOF and LC, events that could be identified to pass the effective area of SDC3 and SDC4 were adopted as the denominator of Eq. (7). The position dependence of $\varepsilon_{\mathrm{SDC34}}$ was negligibly small. The typical value of $\varepsilon_{\mathrm{SDC34}}$ was (96±1)%.

On the other hand, for the case of SDC12, there were no other detectors to define the track to pass the effective area of SDC1 and SDC2. Therefore, events in which the most downstream plane of SDC2 (SDC2X plane) had hits were used. If a source point of the track was the target and SDC2X had a true hit, this tag meant that a particle had passed through the chamber's effective volume. Strictly speaking, the true efficiency ($\varepsilon_{\mathrm{SDC12}}$) and the efficiency estimated in this manner ($\varepsilon_{\mathrm{est}}$) are different, and are written as

$$\varepsilon_{\mathrm{SDC12}} = \varepsilon_{\mathrm{tag}}\varepsilon_{\mathrm{est}} + (1 - \varepsilon_{\mathrm{tag}})\varepsilon_{\mathrm{noest}} ,$$

where $\varepsilon_{\mathrm{tag}}$ is the efficiency for SDC2X plane and $\varepsilon_{\mathrm{noest}}$ is the efficiency under the condition that the SDC2X plane does not fire. The $\varepsilon_{\mathrm{tag}}$ was more than 92% during the experiment and $\varepsilon_{\mathrm{est}}$ was estimated to be about 80%. The difference between $\varepsilon_{\mathrm{SDC12}}$ and $\varepsilon_{\mathrm{est}}$ is less than 1% even if the $\varepsilon_{\mathrm{noest}}$ was taken to be 70% as an extreme case. The small position dependence was included in the error. The typical value of $\varepsilon_{\mathrm{SDC12}}$ was 82±3%.

$\varepsilon_{\mathrm{SKS\ track}}$ and $\varepsilon_{\mathrm{SKS\ cut}}$ were calculated using a similar procedure. Pions which decayed into muons were in some part accepted in these cuts. This effect was taken account of in the calculation of the effective solid angle. These efficiencies were low at the edge of spectrometer acceptance. As a result, they had a strong dependence on the scattering angle.

C. Effective solid angle of the spectrometer

The effective solid angle [$\Delta\Omega_{\mathrm{eff}}(\theta)$] was calculated by a Monte Carlo simulation code GEANT [10]. The effects

TABLE III. Comparison about the choice of shape. The last column gives the summed counts over the range from −3 to 5 MeV in the excitation-energy histogram. Shape 1 is the best of all.

	Shape 1		Shape 2		Shape 3		Counts
	χ^2	Area	χ^2	Area	χ^2	Area	
8°–9°(610)	1.067	5613.1	1.825	5567.3	1.737	5394.8	5632
7°–8°(710)	1.118	8701.6	1.933	8658.0	1.617	8368.0	8648
6°–7°(790)	1.206	10638	1.706	10638	1.595	10260	10562
6°–7°(895)	1.215	14799	2.694	14728	2.541	14232	14639

of the energy loss, multiple scattering, and pion decay to a muon were included. The distributions of the position, direction, and momentum of the beam in the event generator were chosen so as to reproduce the experimental beam profile. Events were generated uniformly from $\theta - \frac{1}{2}\Delta\theta$ to $\theta + \frac{1}{2}\Delta\theta$ with respect to the polar angle and from 0 to 2π with respect to the azimuthal angle. The effective solid angle was calculated using

$$\Delta\Omega'_{\rm eff}(\theta) = \left(\int_{\theta-\frac{1}{2}\Delta\theta}^{\theta+\frac{1}{2}\Delta\theta} d\cos\theta \int_0^{2\pi} d\phi \right) \frac{\text{number of events accepted in the trigger condition}}{\text{number of events generated}} . \quad (8)$$

Pion-decay events should be included in the numerator, since $\varepsilon_{\rm SKS\ track}$ and $\varepsilon_{\rm SKS\ cut}$ were estimated by using the events including decay events.

Pions were absorbed in the material along the track. "Absorb" means that pions are absorbed or scattered to large angles — true absorption, quasifree process, etc. This attenuation ($\varepsilon_{\rm abs}$) was estimated to be about 7%, assuming that the cross sections for these processes are 25 mb, 180 mb, 220 mb, and 320 mb for ^{1}H, ^{12}C, ^{16}O, and ^{28}Si, respectively. Since the horizontal direction of the beam (X') is most sensitive to the shape of the acceptance, the possible change in the solid angles from the shift in the X' distribution of ±3.5 mrad, which almost corresponds to the angular resolution, were taken into account in the systematic error.

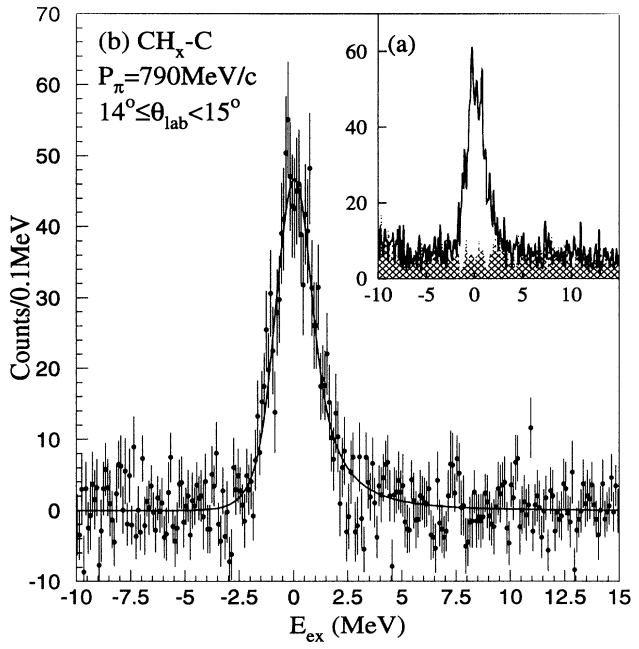

FIG. 4. Excitation energy spectrum for ^{1}H(π^-,π^-) at 790 MeV/c. The scattering-angle range is from 14° to 15°. (a) Raw spectra taken with scintillator (CH_x) target and natural carbon target (hatched area). (b) Histogram subtracted carbon contribution from the spectrum with the scintillator target. The solid line shows the result of fitting with the shape 1 peak.

TABLE IV. Differential cross section for ^{12}C(π^-,π^-) at $P_{\rm lab}$=610 MeV/c. The data from 5.8° to 12.1° were measured in angular setup 1, from 13.2° to 25.8° were in angular setup 2, and from 26.9° to 51.9° were in angular setup 3.

$\theta_{\rm c.m.}$ (deg)	$\frac{d\sigma}{d\Omega}$ (mb/sr)	Statistical error	Systematic error
5.8	307	7.9	48
6.9	306	5.6	36
7.9	299	4.5	31
9.0	271	3.7	25
10.0	248	3.2	21
11.1	233	3.1	20
12.1	208	2.9	18
13.2	194	0.7	20
14.2	162	0.6	15
15.3	133	0.5	12
16.3	108	0.4	9.7
17.4	85.2	0.39	7.7
18.4	67.9	0.35	6.1
19.5	53.1	0.32	4.8
20.6	41.0	0.28	3.7
21.6	31.5	0.26	2.9
22.7	23.8	0.24	2.2
23.7	18.0	0.23	1.2
24.8	12.5	0.22	1.3
25.8	8.32	0.22	1.01
26.9	5.79	0.23	0.96
27.9	3.89	0.15	0.52
29.0	2.27	0.093	0.25
30.0	1.35	0.064	0.14
31.0	0.890	0.047	0.086
32.1	0.583	0.037	0.057
33.1	0.523	0.034	0.049
34.2	0.569	0.034	0.052
35.2	0.538	0.033	0.050
36.3	0.622	0.033	0.058
37.3	0.803	0.040	0.074
38.4	0.772	0.039	0.071
39.4	0.740	0.038	0.068
40.4	0.708	0.038	0.066
41.5	0.690	0.038	0.064
42.5	0.599	0.037	0.055
43.6	0.558	0.036	0.054
44.6	0.518	0.036	0.050
45.6	0.525	0.038	0.053
46.7	0.399	0.035	0.039
47.7	0.387	0.038	0.040
48.8	0.298	0.038	0.035
49.8	0.319	0.046	0.038
50.8	0.284	0.049	0.041
51.9	0.192	0.055	0.038

IV. RESULTS AND DISCUSSION

The differential cross sections for π^--^{12}C elastic scattering are listed in Tables IV–VII. The systematic error includes the absolute normalization error (about 10%). The systematic errors caused by uncertainties of the efficiencies are listed in Table II for the case of angular setup 2 at 790 MeV/c as a typical example. Other errors are 4% from the peak-shape uncertainty and 1.2% from the uncertainty of the target thickness. (Figures 6–9 below also show the angular distributions at each incident momentum. In these figures the error bars represent the quadratic sum of the statistical and systematic errors.)

Figure 5 shows the $\pi^- - p$ differential cross section measured in angular setup 2 using a scintillator target. The solid lines show the results of a phase-shift analysis calculation of SAID [11]. The dashed lines represent those with a Höhler's phase shift [12]. The agreement of the calculations with our data means that our deduction for the absolute magnitude of the cross section is appropriate.

Further, we can confirm the reliability of our data by checking the internal consistency. We have the data in the overlapped angular region between angular setups 1 and 2 for a carbon target. In angular setup 2 we have carbon data from a carbon target and a scintillator tar-

TABLE V. Differential cross section for ^{12}C(π^-,π^-) at $P_{\rm lab}$=710 MeV/c. The data from 5.9° to 14.3° were measured in angular setup 1, from 15.4° to 24.9° were in angular setup 2, and from 26.0° to 49.1° were in angular setup 3.

$\theta_{\rm c.m.}$ (deg)	$\frac{d\sigma}{d\Omega}$ (mb/sr)	Statistical error	Systematic error
5.9	444	6.9	62
6.9	407	5.0	43
8.0	355	4.0	32
9.0	315	3.3	26
10.1	268	2.9	21
11.2	228	2.7	18
12.2	190	2.5	15
13.3	154	2.3	12
14.3	114	2.0	9.0
15.4	90.3	0.35	8.0
16.5	67.1	0.31	5.9
17.5	48.0	0.27	4.2
18.6	33.6	0.23	3.0
19.6	23.0	0.19	2.0
20.7	15.4	0.16	1.4
21.8	10.4	0.14	0.95
22.8	6.85	0.13	0.65
23.9	4.01	0.11	0.41
24.9	2.20	0.11	0.26
26.0	1.10	0.11	0.18
27.1	0.706	0.068	0.102
28.1	0.388	0.038	0.048
29.2	0.346	0.032	0.037
30.2	0.363	0.030	0.036
31.3	0.420	0.030	0.040
32.3	0.559	0.033	0.053
33.4	0.650	0.035	0.061
34.4	0.668	0.035	0.063
35.5	0.714	0.037	0.067
36.5	0.598	0.033	0.057
37.6	0.615	0.034	0.058
38.6	0.476	0.031	0.045
39.7	0.414	0.031	0.039
40.7	0.367	0.030	0.035
41.8	0.272	0.023	0.026
42.8	0.234	0.021	0.023
43.9	0.141	0.018	0.014
45.0	0.0930	0.0151	0.0091
46.0	0.0733	0.0152	0.0076
47.0	0.0563	0.0156	0.0059
48.1	0.0425	0.0155	0.0046
49.1	0.0549	0.0200	0.0067

TABLE VI. Differential cross section for ^{12}C(π^-,π^-) at $P_{\rm lab}$=790 MeV/c. The data from 5.9° to 12.3° were measured in angular setup 1, from 13.4° to 26.2° were in angular setup 2, and from 27.2° to 50.4° were in angular setup 3.

$\theta_{\rm c.m.}$ (deg)	$\frac{d\sigma}{d\Omega}$ (mb/sr)	Statistical error	Systematic error
5.9	436	5.4	53
7.0	405	4.0	42
8.0	355	3.3	30
9.1	306	2.7	25
10.2	253	2.4	20
11.2	207	2.2	16
12.3	160	1.9	13
13.4	122	0.4	13
14.4	82.9	0.31	7.4
15.5	56.4	0.26	5.1
16.6	36.6	0.22	3.3
17.6	22.9	0.17	2.0
18.7	14.2	0.14	1.3
19.8	7.80	0.11	0.72
20.8	4.10	0.082	0.38
21.9	1.84	0.059	0.17
23.0	0.677	0.040	0.063
24.0	0.207	0.025	0.020
25.1	0.157	0.025	0.017
26.2	0.362	0.049	0.044
27.2	0.550	0.087	0.103
28.3	0.843	0.048	0.105
29.3	0.822	0.040	0.086
30.4	0.831	0.037	0.086
31.5	0.759	0.033	0.075
32.5	0.747	0.032	0.074
33.6	0.713	0.031	0.069
34.6	0.575	0.028	0.056
35.7	0.460	0.025	0.045
36.7	0.330	0.022	0.033
37.8	0.265	0.020	0.028
38.9	0.185	0.020	0.018
39.9	0.153	0.025	0.026
41.0	0.0852	0.0114	0.0083
42.0	0.0465	0.0087	0.0045
43.1	0.0241	0.0060	0.0024
44.1	0.00629	0.00471	0.00062
45.2	0.00489	0.00326	0.00048
46.2	0.00199	0.00140	0.00020
48.3	0.00548	0.00411	0.00061
49.4	0.00725	0.00544	0.00087
50.4	0.00984	0.00738	0.00138

TABLE VII. Differential cross section for $^{12}C(\pi^-,\pi^-)$ at P_{lab}=895 MeV/c. The data from 5.9° to 15.6° were measured in angular setup 1 and from 16.7° to 24.2° were in angular setup 2.

$\theta_{c.m.}$ (deg)	$\frac{d\sigma}{d\Omega}$ (mb/sr)	Statistical error	Systematic error
5.9	468	5.2	70
7.0	460	3.9	55
8.1	412	3.1	41
9.2	334	2.4	30
10.2	258	2.0	22
11.3	184	1.7	15
12.4	128	1.4	11
13.5	82.2	1.2	6.8
14.6	50.2	0.93	4.2
15.6	29.9	0.74	2.5
16.7	14.2	0.13	1.2
17.8	6.55	0.096	0.56
18.9	2.61	0.064	0.22
19.9	0.670	0.036	0.057
21.0	0.145	0.026	0.013
22.1	0.185	0.021	0.016
23.1	0.484	0.033	0.044
24.2	1.10	0.056	0.11

get. We found that the agreement in these comparisons was within the statistical errors.

The dashed lines in Figs. 6–9 show PIPIT [13] calculations. PIPIT is a momentum space optical potential code for pion based on a first-order optical potential model factorized as $t\rho$. In this calculation, we used (1) Höhler's phase shift up to the h wave, (2) the sum of Gaussians (SOG) density distribution by Sick [14] as proton and neutron densities in ^{12}C, (3) a Gaussian-type off-shell

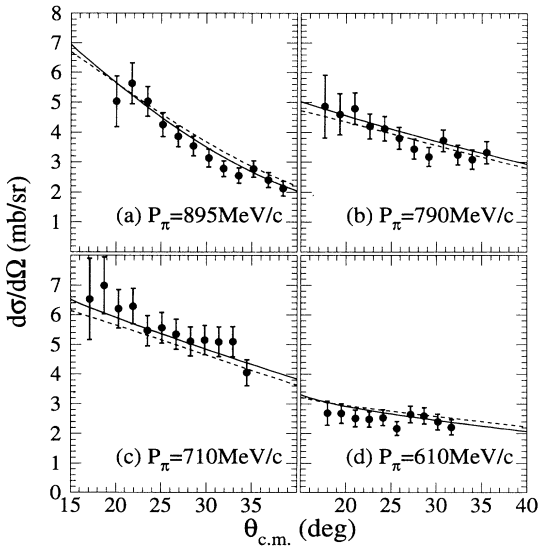

FIG. 5. Differential cross section for π^-p at each incident momentum measured with the scintillator target. The solid lines show the results of SAID calculations and the dashed lines show the results of phase-shift calculations with the Höhler's phase-shift value.

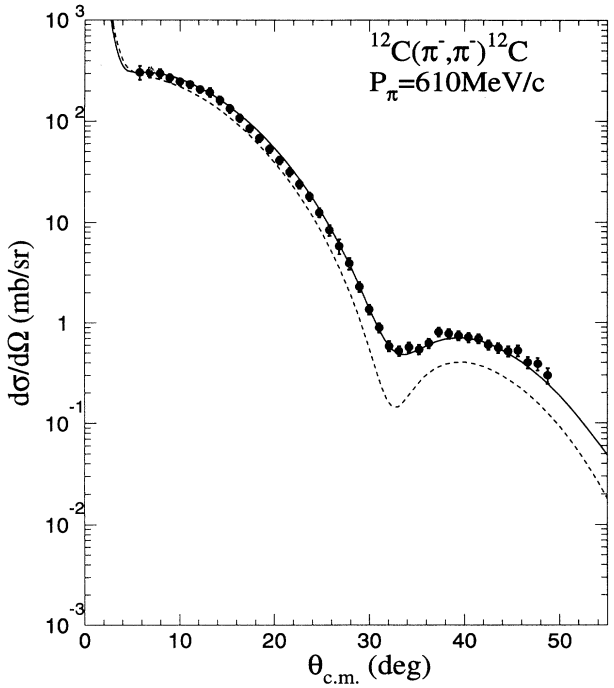

FIG. 6. Differential cross section for $^{12}C(\pi^-,\pi^-)$ at P_π=610 MeV/c. The dashed curves are from PIPIT calculations with free elementary amplitudes, while the solid curve shows the result of a fitting.

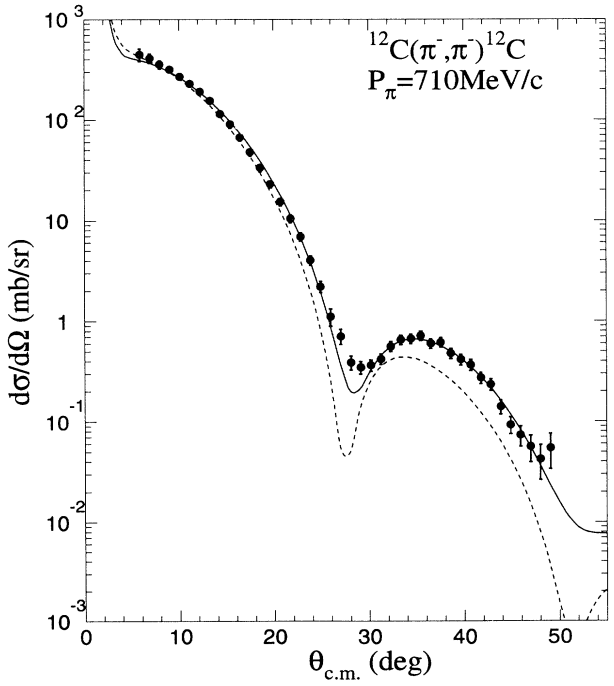

FIG. 7. Differential cross section for $^{12}C(\pi^-,\pi^-)$ at P_π=710 MeV/c.

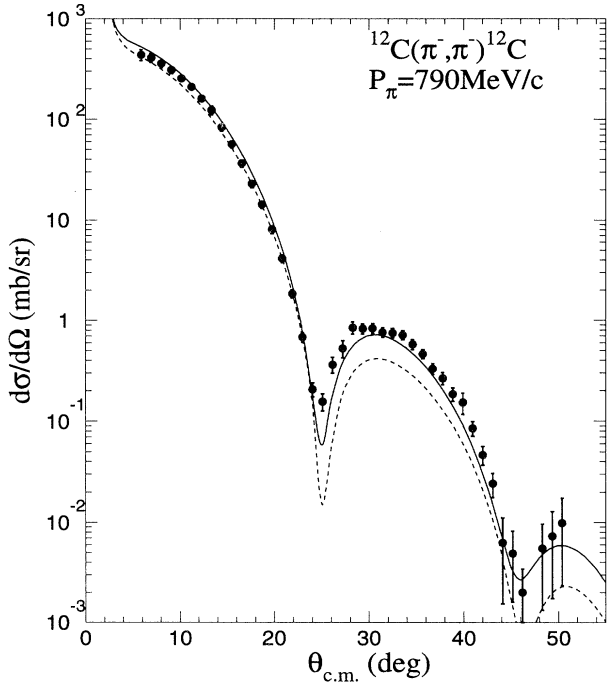

FIG. 8. Differential cross section for $^{12}C(\pi^-,\pi^-)$ at P_π=790 MeV/c.

extrapolation of the t matrix, and (4) a nucleon form factor of $G(t) = [1.0 - t/0.71\ (\mathrm{GeV}^2)]^2$ [15] for unfolding the point nucleon densities from the nuclear density distribution.

At 610 MeV/c, the calculation underestimates the experimental data over the entire angular region. In the forward region ($\theta_{c.m.} \leq 15°$) at other incident momenta, however, PIPIT calculations almost reproduce the magnitudes of the cross sections. At 710 MeV/c, the discrepancy becomes large in the middle angular region ($20° \leq \theta_{c.m.}$). Further, the position of the dip cannot be reproduced. In the second maximum region, the calculations underpredict the data at all of the incident momenta. On the whole, the calculations reproduce well in the forward region as the incident momentum increases.

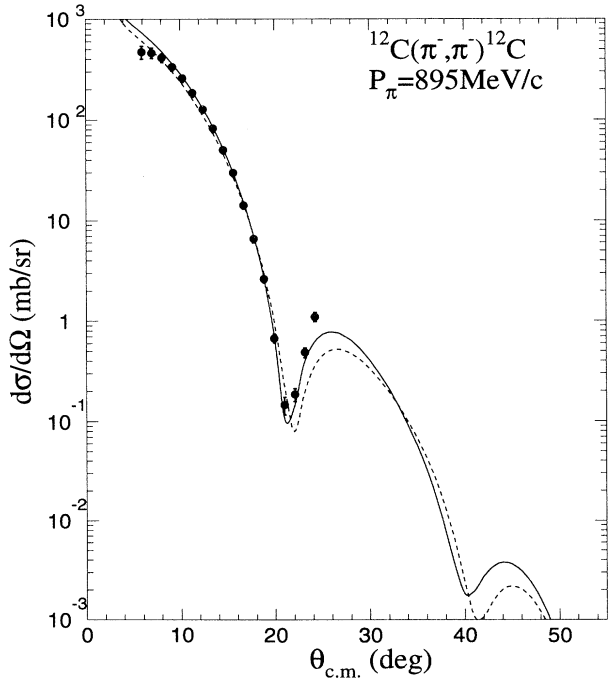

FIG. 9. Differential cross section for $^{12}C(\pi^-,\pi^-)$ at P_π=895 MeV/c.

Our data at 790 MeV/c lie between the BNL data and the theoretical predictions as shown in Fig. 10. Although our data and the BNL data are consistent within the systematic errors (10% and 15%, respectively), a so-called discrepancy between the experiment and the theories at the forward region previously pointed out seems not to be serious. The large discrepancy observed in the backward region may reflect dynamical effects not included in the first-order calculation.

In order to take into account of the dynamical effects, we modified the elementary amplitudes [2,4]. We fitted the angular distributions by modifying the πN elementary amplitudes as follows:

$$\mathrm{Re}\ \tilde{f}^l_{Ij} = a_R\ \mathrm{Re}\ f^l_{Ij}\ ,\quad \mathrm{Im}\ \tilde{f}^l_{Ij} = a_I\ \mathrm{Im}\ f^l_{Ij},$$

where f^l_{Ij} are the free amplitudes and suffixes lIj represent the orbital angular momentum, isospin, and total angular momentum in the total πN system, respectively. The optimum values of a_R and a_I were searched using

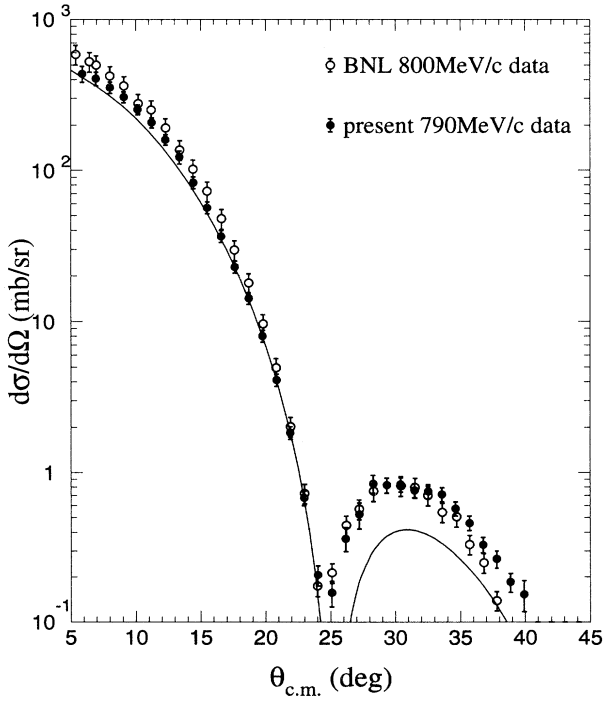

FIG. 10. Comparison of the result of the present work at 790 MeV/c (solid circles) to BNL data at 800 MeV/c (open circles), which are taken from Ref. [1]. The error bars of the BNL data are taken to their normalization error of 15%. The solid line represents the result of PIPIT calculations at 790 MeV/c.

TABLE VIII. The ratio of fitted amplitudes to the free one and extracted cross sections at each incident momentum.

$P_{\rm lab}$ (MeV/c)	a_R	a_I	$\sigma_{\rm tot}$ (mb)	$\sigma_{\rm el}$ (mb)	σ_R (mb)
610	1.46 ± 0.09	0.92 ± 0.05	270.8 ± 8.6	92.2 ± 4.6	178.6 ± 5.9
710	1.59 ± 0.09	0.88 ± 0.04	272.5 ± 8.9	78.1 ± 3.9	194.4 ± 6.0
790	1.36 ± 0.11	1.15 ± 0.05	294.2 ± 8.9	76.3 ± 4.2	217.9 ± 5.0
895	0.90 ± 0.20	1.16 ± 0.05	316.4 ± 11.4	76.7 ± 5.0	239.8 ± 6.4

the MINUIT program [16]. The total cross section ($\sigma_{\rm tot}$), elastic cross section ($\sigma_{\rm el}$), and reaction cross section (σ_R) were extracted from the nuclear part of the scattering amplitude in this model. Since angular distributions were measured in different setups (see Sec. II B), systematic normalization errors among the different setups would change a_R, a_I, $\sigma_{\rm tot}$, σ_R, and $\sigma_{\rm el}$. These values were obtained by the Monte Carlo method: First, we generated the angular distributions by changing the normalization in each setup within their systematic errors. Then optimum values for a_R and a_I were searched for. Repeating these procedures in order to get the distribution of the optimum values a_R, a_I, $\sigma_{\rm tot}$, $\sigma_{\rm el}$, and σ_R, and their errors were evaluated.

The solid lines in Figs. 6–9 present the fitted results; the best-fit values are listed in Table VIII. In Fig. 11 these cross sections are plotted as a function of the incident momentum, together with previously reported data [17–19]. The dashed lines in the figure show the results of a PIPIT calculation with free elementary amplitudes. The experimental data show a different dependence from the calculation. It seems to show that the resonance behavior is smeared out by Fermi motion. Our result shows a different aspect from the photonuclear cross sections for Be and C [20] or the photofission cross sections for Pb and U [21]. In these cross sections, the σ/A in the second [$D_{13}(1520)$] and the third [$F_{15}(1680)$] resonance region is much smaller compared to the free γN cross section.

In order to explain the smooth energy dependence, the effect of Fermi motion was investigated by averaging the elementary amplitudes (f^l_{Ij}) for each partial wave (l, I, j) as follows:

$$\tilde{f}^l_{Ij}(s(0)) = \frac{1}{\frac{4}{3}\pi k_F^3 \Gamma(0)} \int_{k \le k_F} f^l_{Ij}(s(\boldsymbol{k})) \cdot \Gamma(\boldsymbol{k}) \cdot d\boldsymbol{k}, \quad (9)$$

$$s(\boldsymbol{p}_N) = m_\pi^2 + m_N^2 + 2(E_\pi E_N - \boldsymbol{p}_\pi \cdot \boldsymbol{p}_N) \ , \quad (10)$$

where Γ is a g factor in the transformation to the πN c.m. system. In this calculation, k_F of 270 MeV/c was used (nuclear matter). The solid lines in Fig. 11 show the results of a PIPIT calculation using these Fermi-averaged amplitudes. The global energy dependence of $\sigma_{\rm tot}$, $\sigma_{\rm el}$, and σ_R seems to be explained well in this Fermi-averaging model. It seems that the effect of Fermi motion is essential to explain the energy dependence of the total cross section.

For the differential cross section, however, this approximation does not change the shape and the magnitudes much from the calculation using the free amplitude at 610 and 710 MeV/c. At 790 and 895 MeV/c, this calculation reproduces the data better in the forward angular region. The momentum-space first-order optical model calculation by Chen *et al.*, which includes the effects of Fermi motion, etc., does not fully reproduce the angular distribution of the BNL data at 800 MeV/c [3]. A detailed theoretical investigation is necessary.

V. SUMMARY

We measured the differential cross section for ^{12}C(π^-,π^-) at incident pion momenta of 610, 710, 790, and 895 MeV/c, paying attention to obtaining the absolute magnitude precisely. The systematic errors, including the absolute normalization, are about 10%. The $\pi^- p$ differential cross sections, which were measured under the same trigger condition, agree well with the phase-shift calculations.

Although the data at 790 MeV/c are consistent with the BNL data at 800 MeV/c within the systematic errors, our data are in the middle of the BNL data and the first-order factorized momentum-space optical potential calculation. In the forward region, the calculation almost reproduces the magnitude of the cross sections, except at 610 MeV/c, though it underestimates the data in the backward region.

By modifying the elementary amplitudes phenomeno-

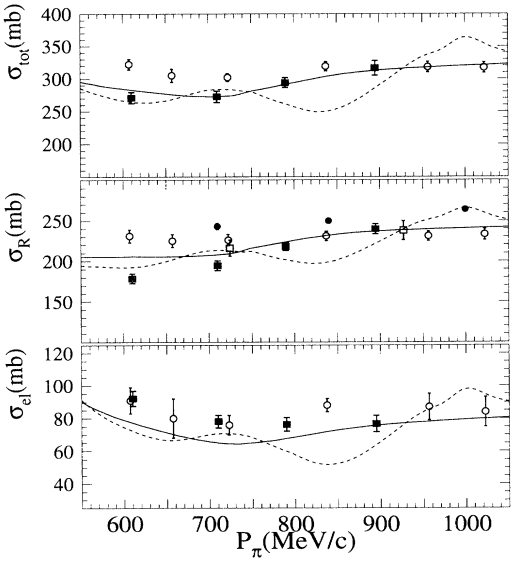

FIG. 11. Incident momentum dependence of (a) $\sigma_{\rm tot}$, (b) σ_R, and (c) $\sigma_{\rm el}$. The data (solid square) are plotted with the data of Crozon *et al.* [19] (open circle), Cronin *et al.* [18] (open square), and Allardyce *et al.* [17] (solid circle). The dashed lines show the result of PIPIT calculations with free amplitudes. The solid lines represent the results taking into account the effect of Fermi motion.

logically, $\sigma_{\rm tot}$, $\sigma_{\rm el}$, and σ_R were extracted. These cross sections show a smoother dependence on the incident energy than does the πN cross section, thus suggesting the importance of Fermi motion effect. For other effects, such as the dynamics and a higher-order contribution, further theoretical investigations are necessary.

ACKNOWLEDGMENTS

We would like to thank the staff of the KEK-PS for their support in running this experiment. Professor K. Nakai, the head of PS experimental planning and program-coordination division, encouraged us during this project. We also thank Dr. M. Ieiri of the KEK-PS beam channel group for advice concerning the beam transport. We wish to acknowledge Professor R. Seki, Professor H. Toki, and Dr. K. Masutani for helpful discussions about theoretical matters during the planning stage. We greatly thank Dr. M. Arima for an offer of the calculation code and discussions. We also thank Y. Sakemi, H. Akimune, and H. Park for their help during the early stage of the experiment.

[1] D. Marlow *et al.*, Phys. Rev. C **30**, 1662 (1984).
[2] M. Arima, K. Masutani, and R. Seki, Phys. Rev. C **44**, 415 (1991).
[3] C. M. Chen, D. J. Ernst, and M. B. Johnson, Phys. Rev. C **48**, 841 (1993).
[4] M. Mizoguchi, K. Sumiyoshi, T. Kajino, and H. Toki, Prog. Theor. Phys. **81**, 1217 (1989); M. Mizoguchi and H. Toki, Nucl. Phys. **A513**, 685 (1990).
[5] V. Franco and H. G. Schlaile, Phys. Rev. C **41**, 1075 (1990).
[6] M. W. Rawool-Sullivan *et al.*, Phys, Rev. C **49**, 627 (1994).
[7] T. Fukuda *et al.*, Nucl. Instrum. Methods (submitted).
[8] K. L. Brown *et al.*, Report No. CERN 74-2, 1974.
[9] J. Myrheim and L. Bugge, Nucl. Instrum. Methods **160**, 43 (1979).
[10] CERN Program Library Entry W5013, GEANT.
[11] R. Arndt, computer code SAID with Summer 1989 solutions.
[12] G. Höhler, in *Pion Nucleon Scattering,* edited by H. Schopper, Landolt-Börnstein, New Series, Group I, Vol. 9b, Pt. 2 (Springer-Verlag, Berlin, 1983).
[13] R. A. Eisenstein and F. Tabakin, Comput. Phys. Commun. **12**, 237 (1979).
[14] I. Sick, Nucl. Phys. **A218**, 509 (1974).
[15] H. Pilkuhm, in *Particle Properties, Coupling Constants and Form Factors,* edited by H. Schopper, Landolt-Börnstein, New Series, Group I, Vol. 6, Pt. 1 (Springer-Verlag, Berlin, 1972).
[16] CERN Program Library Entry D506, MINUIT.
[17] B. W. Allardyce *et al.*, Nucl. Phys. **A209**, 1 (1973).
[18] J. W. Cronin, R. Cool, and A. Abashian, Phys. Rev. **107**, 1121 (1957).
[19] M. Crozon, Ph. Chavanon, A. Courau, Th. Leray, J. L. Narjoux, and J. Tocqueville, Nucl. Phys. **64**, 567 (1965).
[20] M. Anghinolfi *et al.*, Phys. Rev. C **47**, 922 (1993).
[21] N. Bianchi *et al.*, Phys. Lett. B **299**, 219 (1993).